# Theoretical Description of Pseudocubic Manganites

Chungwei Lin and Andrew.J.Millis

*Department of Physics, Columbia University*

*538W 120th St NY, NY 10027*

## Abstract

A comprehensive theoretical model for the bulk manganite system $La_{1-x}(Ca,Sr)_x MnO_3$ is presented. The model includes local and cooperative Jahn-Teller distortions and the on-site Coulomb and exchange interaction. The model is is solved in the single-site dynamical mean field approximation using a solver based on the semiclassical approximation. The model semi-quantitatively reproduces the observed phase diagram for the doping $0 \leq x < 0.5$ and implies that the manganites are in the strong coupling region but close to Mott insulator/metal phase boundary. The results establish a formalism for use in a broader range of calculations, for example on heterostructures.

PACS numbers: 71.10-w,71.30.+h,75.10.-b

arXiv:0808.0736v2 [cond-mat.str-el] 24 Oct 2008

## I.  INTRODUCTION

LaMnO$_3$ crystallizes in a structure closely related the basic ABO$_3$ perovskite form. As the temperature is varied it undergoes orbital ordering and antiferromagnetic transitions. Replacing some of the La by divalent alkali ions such as Ca yields an even wider range of phenomena, including charge ordering, ferromagnetism, and colossal magnetoresistance [**? ? ?** ]. The phase diagram is summarized in Fig(1). While the manganites have been studied for many years, and much of the physics has been understood, there is as yet no consensus in the literature on a model which is rich enough to account for all the physics, includes all of important interactions, and can be solved to predict (or at least explicate) new phenomena such as those occurring in systems such as heterostructures. In this paper we develop such a model and explore its properties. Our results place the materials in the strong/intermediate coupling regime.
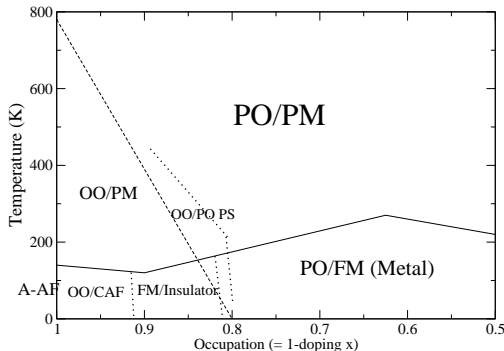


FIG. 1: The experimental phase diagram as a function of doping $x$ and temperature $T$. PO: paraorbital; PM: paramagnetic; FM: ferromagnetic; OO: orbitally ordered; AAF: A-type antiferromagnetic. See text for the descriptions of the phases.

The phase diagram shown in Fig(1) includes two magnetic orders, A-type antiferromagnetic (A-AFM) and ferromagnetic (FM) states, corresponding to the Mn spin arrangements shown in Fig(2). The A-AFM structure consists of ferromagnetic planes antiferromagnetically coupled. With our coordinate choice, each FM plane is spanned by $\hat{x}$ and $\hat{y}$ while the remaining direction is $\hat{z}$. The orbital order (OO) in this context refers to a particular distortion arrangement where the oxygen octahedra have in-plane staggered ($x - y$ plane) $Q_x$ JT distortions plus a uniform $-Q_z$ distortion (the minus sign represents the octahedron shrinking in $z$ while expanding in $x - y$ directions) (Fig(2)). The metal/insulator phase boundary
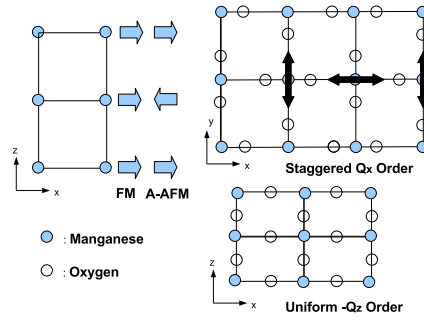
2

FIG. 2: (Color online) Illustrations of FM, A-AFM, and orbital orders. The filled and open circles represent manganese and oxygens respectively. The light arrows stand for the core-spin orientation at each plane. Upper left panel: illustration of two magnetic orders. For FM, the spins at different planes are aligned in the same direction while for A-AFM, the spins at adjacent planes arranged oppositely. Upper right panel: illustration of the in-plane staggered $Q_x$ order is shown in the up-right corner. The double-arrows represent the long O-Mn-O distance caused by the $Q_x$ distortion. Lower panel: illustration of the uniform $-Q_z$ order: the system uniformly shrinks in the $z$ direction while it expands in $x - y$.

is determined from the DC resistivity. The definition of metal/insulator is ambiguous. Here we adopt the definition that the system is metallic/insulating at a given *temperature* if the temperature derivative of resistivity is positive/negative.

In this paper, we present a model which captures all of the physics discussed above and solve it by the single-site dynamical mean field theory (DMFT)[? ]. There are two main purposes for this study. First, although basic understanding for exhibited phases at a *given* doping is known, it is important to determine the extent to which the general model with **a fixed set of parameters** matches the observed phase diagram. Second, we wish to apply this theory to understand the behavior of the recently synthesized manganite superlattices [? ? ].

Solving a theoretical model ordinarily requires approximations. Here we use the single site DMFT[? ]. This approximation requires as an intermediate step the solution of a quantum impurity model. In this paper we solve the impurity model using a generalization of the semiclassical approximation (SCA) [? ]. We generalize it to the 2-band case and develop a formalism for incorporating the cooperative Jahn-Teller (JT) effect into the single-

site DMFT. We semiquantitatively reproduce the observed phase diagram for $0 < x < 0.5$ and identify the sources of the observed phases. Our calculation yields three main results. First, our calculation suggests the problem is in the "strong/intermediate" coupling regime in the sense that under the single-site DMFT approximation the local interaction strength is slightly larger than the critical value needed to drive a metal-insulator transition. Consequently the system is very sensitive to the mechanisms governing the bandwidth such as magnetic order and details of crystal structure. Second, the cooperative Jahn-Teller effect is the main source accounting for the observed high orbital ordering temperature. Finally, our calculation confirms that when the doping is increased to the colossal magneto-resistance (CMR) region $x \sim 0.3$ ($N \sim 0.7$), the double-exchange (DE) mechanism becomes dominant.

The rest of the paper is organized as follows. We first present the model and the interactions included. After providing key steps for our approximation, we show how we fit parameters and then present the results. Discussion concerning the inadequacies of our model/approximation and differences between the calculation and the experiments is given in Section VII. Section VIII is a conclusion. In the appendices we examine the validity of the SCA approximation and give details of the procedure we use to take the cooperative Jahn-Teller effect into account.

## II.   MODEL HAMILTONIAN

In this section we describe the interactions included in our model and define terms and notations which shall be used for the rest of the paper.

*Tight-binding*: The band structure is described by a tight-binding model where only nearest neighbor hopping between $e_g$ orbitals is included. A justification for this approximation is given in [**?** ]. Two $e_g$ orbitals are labeled as $|1\rangle = |3z^2 - r^2\rangle$, $|2\rangle = |x^2 - y^2\rangle$. This implies a band Hamiltonian which may be written as

$$H_{band} = \sum_{\vec{k},ab,\sigma} \epsilon_{\vec{k},ab,\sigma} c^{\dagger}_{\vec{k},a,\sigma} c_{\vec{k},b,\sigma} \tag{1}$$

$\epsilon_{\vec{k},ab,\sigma} = -t(\varepsilon_0 \hat{e} + \varepsilon_z \hat{\tau}_z + \varepsilon_x \hat{\tau}_x)_{ab}$ where $\hat{\tau}$ 's are Pauli matrices, $\hat{e}$ is the unit matrix and $\varepsilon_0 = \cos k_x + \cos k_y + \cos k_z$, $\varepsilon_z = \cos k_z - \frac{1}{2}(\cos k_x + \cos k_y)$, and $\varepsilon_x = \frac{\sqrt{3}}{2}(\cos k_x - \cos k_y)$. $a, b$ label orbitals, $i, j$ sites, and $\sigma$ spins. We emphasize that what denoted here as two $e_g$ orbitals are actually the anti-bonding combination of Mn $3d$ and its neighboring oxygen

$2p(\sigma$ bond) states [? ].

*On-site e-e*: For the on-site interaction within $e_g$ orbitals, we use the Goodenough-Kanamori-Slater approximation in which the form of interaction is the same as in the free atom. Two independent parameters conventionally denoted as $U$ and $J$ are required to specify this interaction. It is generally accepted[? ] that the charging energy $U$ may be strongly renormalized by solid state effects whereas the inter-orbital exchange energy $J$ is less affected. The e-e interaction within the $e_g$ multiplet is

$$H_{EE} = \sum_{\sigma,\sigma'}(U-J)n_{1,\sigma}n_{2,\sigma'} + U\sum_{i=1,2}n_{i,\uparrow}n_{i,\downarrow} + J(c_{1,\uparrow}^\dagger c_{1,\downarrow}^\dagger c_{2,\downarrow}c_{2,\uparrow} + h.c.) - 2J\vec{S}_1 \cdot \vec{S}_2 \quad (2)$$

where $\vec{S}_{1(2)} = \vec{\sigma}_{\alpha\beta}c_{1(2),\alpha}^\dagger c_{1(2),\beta}$. The $J(c_{1,\uparrow}^\dagger c_{1,\downarrow}^\dagger c_{2,\downarrow}c_{2,\uparrow} + h.c.)$ term is referred to as the pair hopping and the $-2J\vec{S}_1 \cdot \vec{S}_2$ term is the exchange.

*Hund's coupling*: The coupling between Mn $e_g$ and Mn $t_{2g}$ electrons is approximated by $H_{Hund}$ in which three $t_{2g}$ electrons are treated as an electrically inert "core spin" of magnitude $S = (3/2)\hbar$. We shall further approximate the core spin as classical and normalize $J_H$ by taking $|\vec{S}| = 1$, leading to

$$H_{Hund} = -J_H \sum_i \vec{S}_i \cdot c_{i,\alpha}^\dagger \vec{\sigma}_{\alpha\beta}c_{i,\beta} \quad (3)$$

where $J_H > 0$ and $|\vec{S}| = 1$. The minus sign ensures that the high spin state is energy-favored in accordance with the Hund's rule.

*Lattice elastic energy*: For the lattice degree of freedom, we consider Mn motions in arbitrary directions($\vec{\delta}_i$) and oxygen only along Mn-O ($\sigma$) bond direction ($u_{i,x}$) [? ? ] where $\vec{\delta}_i$ and $u_{i,x}$ are illustrated in Fig(3). The general lattice elastic energy in the harmonic approximation is

$$H_{lat} = \frac{1}{2K_{M-O}} \sum_{i,a}[(\delta_i^a - u_i^a)^2 + (\delta_i^a - u_{i-a}^a)^2] \quad (4)$$

$$+ \frac{1}{2}\sum_{\vec{k},ab} E^{ab}(\vec{k})\delta_{\vec{k}}^a\delta_{-\vec{k}}^b + \frac{1}{2}\sum_{\vec{k},ab} D^{ab}(\vec{k})u_{\vec{k}}^a u_{-\vec{k}}^b \quad (5)$$

where $1/K_{M-O}$ is spring constant between neighboring manganese, oxygen, while $E^{ab}(\vec{k})$ and $D^{ab}(\vec{k})$ are general Mn-Mn, O-O couplings in $k$ space. In the specific numerical calculations presented here, we set $E^{ab}(\vec{k}) = 0$ and $D^{ab}(\vec{k}) = \frac{4}{k_{M-M}}\delta^{ab}\sin^2(k_a/2)$, but effects arising from a more general interaction are discussed. With our convention, $u$, $\vec{\delta}$ and lattice constants $K$ all have dimension of energy.
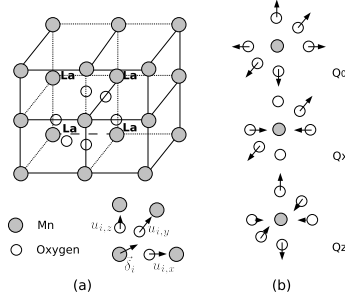
FIG. 3: (a) The ideal cubic perovskite structure for LaMnO$_3$ and the lattice degrees of freedom considered here: Mn can move in arbitrary direction $\vec{\delta}_i$ while oxygen ions only move along the Mn-O bond direction $u_{i,x(y,z)}$. (b) Sketch of the three octahedral distortion modes considered here: $Q_0$ breathing mode, $Q_x$ and $Q_z$ Jahn-Teller modes.

*Electron-Lattice coupling*: The breathing ($Q_0$) and Jahn-Teller (JT) ($Q_x$, $Q_z$) modes at site $i$ are defined by:

$$\begin{aligned}
Q_{i,0} &= \frac{1}{\sqrt{3}}(v_{i,x} + v_{i,y} + v_{i,z}) \\
Q_{i,x} &= \frac{1}{\sqrt{2}}(v_{i,x} - v_{i,y}) \\
Q_{i,z} &= \frac{1}{\sqrt{6}}(-v_{i,x} - v_{i,y} + 2v_{i,z})
\end{aligned} \tag{6}$$

where $v_{i,a} = u_{i,a} - u_{i-a,a}$. The $e_g$ orbitals couple to these three modes as

$$H_{JT} = -\sum_{i,a,b}(Q_{i,x}\tau^x_{ab} + Q_{i,z}\tau^z_{ab})c^\dagger_{i,a}c_{i,b} \tag{7}$$

$$H_B = -\beta Q_{i,0}(n_i - \langle n \rangle) \tag{8}$$

where $\beta$ is dimensionless and positive. We will take $\beta = 1$ which simplifies the discussion of cooperative Jahn-Teller effect. In this paper we treat $H_B$ by a mean field approximation, so it is only important when the charge distribution is not uniform, like in the heterostructures or in the charge-ordered phase. In our definition, positive $Q_z$ stands for the distortion where the octahedron *expands* in the $z$ direction while *shrinking* uniformly in $x - y$ with fixed volume. The minus sign in Eq(7) means that the positive $Q_z$ favors the occupancy of the $|3z^2 - r^2\rangle$ state. This sign choice is justified because positive $Q_z$ increases the lattice constant in $z$ direction and consequently reduces $|t_{pd}|$ and $E_{anti-bonding}$, increasing the occupation in

the anti-bonding band which is mainly composed of Mn $|3z^2 - r^2\rangle$. A similar consideration leads to the minus sign in Eq(8) (positive $Q_0$ means a volume expansion of the octahedron).

*Cubic term in lattice energy*: An anharmonic cubic term [? ] in lattice energy is also included.

$$H_{Cubic} = -A(3Q_{i,z}^3 - Q_{i,x}^2 Q_{i,z})$$ (9)

where $A$ in our convention has the dimension $[E]^{-2}$. Note this is the only cubic combination satisfying the lattice cubic symmetry. With the minus sign, positive $A$ is required to produce the observed distortions for $LaMnO_3$.

*G-type AF coupling*: There is an isotropic nearest neighbor AF coupling (G-type) between $t_{2g}$ spins $\vec{S}_i$.

$$H_{AF} = J_{AF} \sum_{i,\hat{n}} \vec{S}_i \cdot \vec{S}_{i+\hat{n}}$$ (10)

with positive $J_{AF}$. This coupling arises from the super-exchange mechanism (virtual hopping in $t_{2g}$ channels) and experimentally shows in the G-type AF order exhibited in $CaMnO_3$ [? ]. The main effect of this term is to reduce the magnetic transition temperature.

The total Hamiltonian is then

$$H_{tot} = H_{band} + H_{EE} + H_{Hund} + H_{lat} + H_{JT} + H_B + H_{Cubic} + H_{AF}$$ (11)

## III.   METHOD

We use the single-site Dynamical Mean Field Theory (DMFT) with the semiclassical approximation (SCA) to solve this two-orbital problem [? ]. In the DMFT approximation one replaces the full lattice self energy $\Sigma(\omega, \vec{p})$ by a local (momentum-independent) quantity $\Sigma(\omega)$ which is determined from the solution of an auxiliary problem (quantum impurity model) plus a self consistency condition. The multiplicity of orbitals and interactions means that the impurity model is not easy to solve. We use a Hubbard-Strotonovich transformation proposed by Sakai [? ] and the semiclassical approximation. To evaluate the frequency sum we use a procedure recently introduced by Monien [? ].

We also mention two simplifications here. First we do not take into account the Coulomb potential produced by the random distribution of cations – the only effect of replacing some La by divalent elements is to reduce the $e_g$ electron population. However due to

the screening effect from conduction electrons, we believe this simplification is not crucial. Second, we restrict our calculation to charge-uniform states therefore we cannot obtain the charge ordered phase which may be energy favored around half doping.

The rest of this section is organized as follows. Two key ingredients will be discussed: first we show how we encode the cooperative Jahn-Teller effect in the local impurity problem; second we give some detailed formalism about SCA in this 2-orbital problem, especially how we decompose the quartic interaction and what simplifications we have made. Then we discuss what measurements we used to fit parameters.

### A.   Cooperative Jahn-Teller

The local octahedral distortions $(Q_0, Q_x, Q_z)$ at different sites are not independent – distortion at one site inevitably causes distortion at the neighboring sites so that some global configurations of the lattice distortions are energy favored. This is the cooperative Jahn-Teller effect [? ] which correlates the octahedral distortions at different sites. Here we include this inter-site effect into the single-site DMFT by integrating out all of distortion fields except for those involving the variable $v$ at the site of interest. The detailed calculation is given in the appendix A and the resulting local effective potential is

$$V_{eff}(Q_0, Q_x, Q_z) = \frac{Q^2}{2K} + \epsilon \vec{F} \cdot \vec{Q} \tag{12}$$

where $K$ is an effective spring constant, $\epsilon \vec{F}$ represents the force exerted on the distortions at one site by static (mean field) distortions on the other site. Here $\vec{F}$ measures the amplitude of the long ranged order and $\epsilon$ gives the strength of the cooperative Jahn-Teller coupling.

### B.   On-site e-e

The key step in our solution of the impurity model is to rewrite the quartic interaction into sums of complete squares so the continuous Hubbard-Strotonovich transformations can be applied. Using the decomposition proposed by Sakai [? ], we define $f_\sigma \equiv c_{1\sigma}^\dagger c_{2\sigma} + c_{2\sigma}^\dagger c_{1\sigma}$, $n \equiv n_1 + n_2$, $q \equiv n_1 - n_2$, $s \equiv (n_{1,\uparrow} - n_{1,\downarrow}) + (n_{2,\uparrow} - n_{2,\downarrow})$, and $d \equiv (n_{1,\uparrow} - n_{1,\downarrow}) - (n_{2,\uparrow} - n_{2,\downarrow})$, and re-express Eq (2) as

$$H_{EE} = U_0 n - \frac{J}{2}(f_\uparrow - f_\downarrow)^2 + \frac{U_n}{2}n^2 - \frac{U_q}{2}q^2 - \frac{U_s}{2}s^2 - \frac{U_d}{2}d^2 \tag{13}$$

8

with $U_0 = 0$, $U_n = (3U - 5J)/4$, $U_q = (U - 7J)/4$, $U_s = (U + J)/4$, and $U_d = (U - 3J)/4$. Due to the fermionic identity $\hat{n}_{i,\sigma}^2 = \hat{n}_{i,\sigma}$ ($i = 1, 2$ $\sigma = \uparrow, \downarrow$), those coefficients are not unique. For example, $U_0 = J/2$, $U_n = (3U - 6J)/4$, $U_q = (U - 6J)/4$, $U_s = (U + 2J)/4$, and $U_d = (U - 2J)/4$ is another legitimate set of choice. If the impurity problem is solved exactly, these two choices lead to the same result, but if approximate methods are used this needs not to be the case. However in the current study, the coefficients will be determined by fitting to data so this ambiguity is not important.

## C. The Impurity Problem

The impurity problem is then described by the effective action $S = S_0 + S_{int}$ where

$$S_0 = -\int d\tau d\tau' a_{\alpha\beta}^{ij}(\tau - \tau') c_{\alpha,i}^\dagger(\tau) c_{\beta,j}(\tau') \tag{14}$$

and $S_{int} = \int d\tau H_{EE}(\tau)$. The partition function is $Z_{imp} = \int d\vec{Q}\, d\vec{S}\, D[c^\dagger c]\, e^{-S}$. Applying the Hubbard-Stratonovich (HS) transformations [? ] to decouple $H_{EE}$, one arrives

$$
\begin{aligned}
S_{int} =& \int d\tau \left( \frac{1}{2U_n}\phi_n^2(\tau) + \frac{1}{2J}\phi_f^2(\tau) + \frac{1}{2U_q}\phi_q^2(\tau) + \frac{1}{2U_s}\phi_s^2(\tau) + \frac{1}{2U_d}\phi_d^2(\tau) \right) \\
&+ \int d\tau \left( -i\phi_n(\tau)n(\tau) + \phi_f(\tau)(f_\uparrow(\tau) - f_\downarrow(\tau)) + [\phi_q(\tau)q(\tau) + \phi_s(\tau)s(\tau) + \phi_d(\tau)d(\tau)] \right) \\
&+ \int d\tau \left( \vec{Q} \cdot \vec{T}_{ab}\delta_{\alpha\beta} + J_H \vec{S} \cdot \delta_{ab}\vec{\sigma}_{\alpha\beta} \right) c_{i,\alpha}^\dagger(\tau) c_{j,\beta}(\tau)
\end{aligned}
\tag{15}
$$

To maintain the symmetries of the local interaction (SU(2) for spin, U(1) for orbital), we generalize the scalars $\phi_s$, $\phi_q$, to vectors $\vec{\phi}_s$ ($= (\phi_{s,x}, \phi_{s,y}, \phi_{s,z})$, 3 components) and $\vec{\phi}_q$ ($= (\phi_{q,z}, \phi_{q,x})$, 2 components) and average over their directions[? ]. After expressing the $S_{int}$ in frequency space, two simplifications are made. First, only zero frequency component for each HS field ($\phi(i\omega_0) = \phi$) is kept and second, saddle point approximations are applied to $\phi_f$, $\phi_d$, and $Q_0$ fields, i.e. $\phi_f = \phi_d = Q_0 = 0$. Different methods have been proposed for handling the $i\phi_n$ field [? ? ]. For the 2-band model studied here, we found the method of Ref[? ] effectively enhances the local orbital moment as the doping increases which is opposite the observation while the method in Ref[? ] is free from this trouble, therefore we follow Ref[? ] and take $i\phi_n = 0$. After integrating out the fermionic degree of freedom and combining the lattice effect, one gets

$$V_{eff} = \left( \frac{Q^2}{2K} + \frac{\phi_q^2}{2U_q} + \frac{\phi_s^2}{2U_s} \right) + A(3\langle Q_z \rangle^2 - \langle Q_x \rangle^2)Q_z + \epsilon\vec{F} \cdot \vec{Q} - T\sum_{\omega_n} \text{Tr}\log \mathbf{A}(i\omega_n) \tag{16}$$

with

$$\mathbf{A} = \mathbf{a} + (\vec{Q} + \vec{\phi}_q) \cdot \vec{\tau} + (J_H \vec{S} + \vec{\phi}_s) \cdot \vec{\sigma} \tag{17}$$

where $\mathbf{A}$ is a $4 \times 4$ matrix and $\mathbf{a}$ the Weiss function. The $A(3\langle Q_z \rangle^2 - \langle Q_x \rangle^2)Q_z$ term comes from the simple mean field approximation of the cubic lattice energy.

### D.  Parameters and Fitting

The discussion above indicates that there are seven parameters to be determined: the hopping $t$, effective local JT coupling $U_Q$, effective magnetic coupling $U_s$, Hund's coupling $J_H$, core-spin AF coupling $J_{AF}$, cooperative JT coefficient $\epsilon$, and anharmonic lattice energy $A$. The first six have the dimension of energy (E) and will be measured in units of the hopping $t$ while the last one has dimension $1/\text{E}^2$.

The hopping strength $t$ has been determined from the band structure calculation for the experimental observed structure of $LaMnO_3$ to be roughly 0.5eV ($\sim$5000 K) [? ]. By contrast, the value appropriate to the ideal perovskite structure is roughly 0.65eV. The difference is due mainly to the effect of the $GdFeO_3$ rotation. For the series $La_{1-x}Ca_xMnO_3$ the distortion depends weakly on the doping $x$ (less than 10%). For $La_{1-x}Sr_xMnO_3$ the rotation angle is more $x$-dependent (up to 30%). Therefore calculations in which $t$ is taken to be independent of $x$ may be appropriate for the Ca series but are unlikely to be adequate for the Sr series. We focus here on the Ca series. We note that the value $t = 0.5$eV is in good agreement with the spectral weight inferred from the optical conductivity experiments on the ferromagnetic phase of $La_{0.7}Ca_{0.3}MnO_3$ [? ]. The $J_{AF}$ is estimated from the Neel temperature of $CaMnO_3$, roughly $110K \sim 0.01$eV [? ]. The $T_N$ of the Heisenberg model $H = \sum_{i,j} J_{AF} \frac{9}{4} \vec{S}_i \cdot \vec{S}_j$ with $|\vec{S}| = 3/2$ obtained from simple mean field is $\frac{20}{9} J_{AF}$, from which we estimate $J_{AF} \sim 4.5$meV$\sim 0.009t$. The super-exchange argument (from virtual hopping of $t_{2g}$ electrons)[? ] also leads to the same estimate. We further found that within the mean field approximation, $J_{AF}$ term only acts to reduce to magnetic transition temperatures by 5-10% but does not result in any new magnetic order. Including this term however substantially increases the calculation time, so we typically set $J_{AF} = 0$ to accelerate the converging processes. The anharmonic lattice energy is taken to be $A = 0.006t^{-2}$ so that our calculation reproduces the observed JT distortion around room temperature for $LaMnO_3$ [?

].

The remaining parameters $J_H$, $U_s$, $U_Q$, $\epsilon$ are fitted by comparing the calculated and observed optical conductivity in LaMnO$_3$. Generally the $\sigma(\omega)$ contains peaks corresponding to local excitation energies of the system. If we treat the hopping $t$ as a small perturbation, then peaks in the optical conductivity are roughly the energy differences between the excited states and the ground state of the *local* Hamiltonian. Since there are 4 states (2 spins $\times$ 2 orbitals) at each site, we expect there are 3 main peaks in $\sigma(\omega)$ corresponding to three 2-electron final states. The saddle point estimate from the local potential indicates these three peaks are located at $2U_Q(1+\epsilon)$ (correct spin, other orbital), $2(J_H + U_s)$ (same orbital, antiparallel spin), and $2U_Q(1 + \epsilon) + 2(J_H + U_s)$ (other orbital, antiparallel spin) which essentially agrees with our calculated results shown in Fig(5). The issue is discussed further in Ref[**?** ]. Experimentally there are two apparent peaks observed in LaMnO$_3$ [**?** ] – the lower one around 2eV ($\sim 4t$) while the higher around 4eV ($\sim 8t$). There are several minor structures around 5-6eV which we do not consider. Fitting the two main peaks in optical data suggests $U_Q(1 + \epsilon) \sim 4(t)$, $J_H + U_s \sim 8(t)$. We choose $J_H = 2.8$, $U_s = 1.4$, $U_Q = 2.1$, $\epsilon = 0.05$. We found that if $J_H + U_s$ is fixed the relative values of $J_H$ and $U_s$ do not change the result much as long as $U_Q > U_s$. If $U_Q < U_s$, the orbital order is not stable against the magnetic order. Since at $T = 0$ the SCA reduces to the simple mean field approximation where expectation values are determined by their saddle point values, the combination $U_Q(1+\epsilon)$ uniquely determines the $T = 0$ phase. However $\epsilon$ has more significant effect on the non-zero temperature phase. We choose $\epsilon$ so as to produce the observed $T_{oo}$.

*Standard parametrization*: Unless indicated otherwise the results we shall present later correspond to our standard parameters $t = 0.5$eV, $U_Q = 2.1t$, $U_s = 1.4t$, $J_H = 2.8t$, $J_{AF} = 0$, $\epsilon = 0.05$, $A = 0.006/t^2$. We remind the reader that this choice of $t$ is only appropriate for Ca doped materials; in the Sr series the $t$ changes with doping. All the temperature, frequency are measured in $t$; a simple conversion $0.5$eV$\sim 5500K$.


## IV.  THE PHASE DIAGRAM

The calculated phase diagram as a function of doping and temperature is shown in Fig(4) The results qualitatively reproduce the observed phase diagram (Fig(1)) in the sense that the relative positions of calculated magnetic/orbital phases are consistent with the experiments,

11

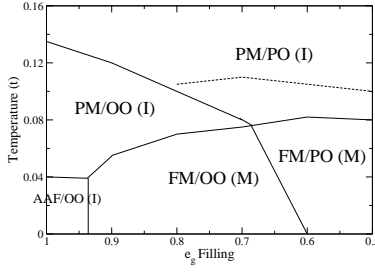but the temperature scales are larger than observed.



FIG. 4: Calculated phase diagram as a function of doping $x$ and Temperature. M and I stand for metallic and insulating phases. The dashed curve is the PM/FM phase boundary, computed using $t = 0.6$eV appropriate to $La_{0.6}Sr_{0.4}MnO_3$.

According to the doping, we divide the phase diagram into three regions – the undoped case ($x = 0$, $LaMnO_3$), the CMR regime ($0.3 < x < 0.5$), and the crossover regime ($0 < x \leq 0.3$). In essence, the undoped case is cooperative JT dominated and the signature is the lattice distortions or equivalently the orbital order. On the other hand, the CMR regime is double-exchange (DE) dominated in which the system is FM/metallic at low temperature. In the crossover regime, both mechanisms play non-negligible roles to the system and we see that as doping increases, the cooperative JT effect decreases ($T_{oo}$ decreases) while the DE mechanism gradually takes over ($T_c$ increases). In principle, we can extend our calculation to $x > 0.5$. However this region the effect of G-type AF coupling $J_{AF}$ starts to emerge (or both double-exchange and cooperative JT effect decreases) and a different self-consistency condition (G-AF) is required, so we shall leave it for future study.

The remainder of the paper is organized as follows. We shall devote one section for the undoped case and one for the CMR and crossover region for more detailed discussions, then discuss the discrepancies between calculated and observed results. What important physics we are missing in our model/approximation and their effects to the current results will be stated. We also point out here that for the spectral functions we shall present, the fermi energy is at zero. Without further indications, $\rho$, $\sigma$ and $A$ stand for resistivity, conductivity, and spectral function respectively.

## V. THE UNDOPED CASE

### A. Overview

Experimentally LaMnO$_3$ is insulating for all temperatures at least up to 800K [? ? ? ] , which is slightly greater than the orbital ordering temperature $T_{oo}$. When the temperature is lowered, it first goes from PO/PM to OO/PM at $T_{oo} \sim 780K(0.135t)$, then from OO/PM to OO/AFM at $T_{AAF} \sim 140K(0.04t)$ where temperatures in Kelvin are experimentally derived while numbers in parentheses are from calculation. After a discussion about the nature of the insulating behavior, we examine the physical origins of the exhibited phases.

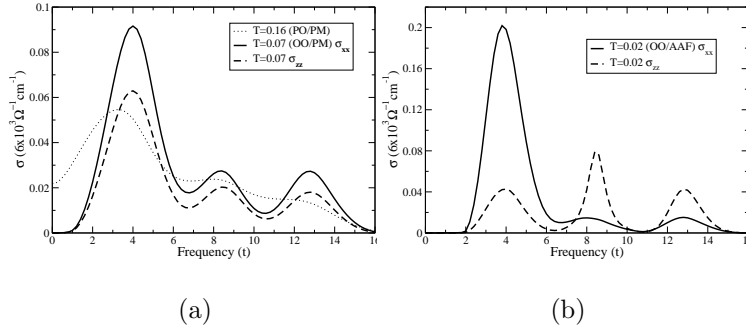### B. The Transport and Excitation Spectrum



(a) (b)

FIG. 5: Optical conductivities for (a) $T = 0.16t(> T_{oo})$ (dotted) $T = 0.07 \sim 0.5T_{oo}$, OO/PM phase and (b) $T = 0.02t \sim 0.5T_{AAF}$, OO/AAF phase. The heavy solid/dashed curves represent the in-plane/out-of-plane optical optical conductivities. To convert the frequency scale to physical units we note that the band theory indicates $t = 0.5$eV so $t = 4$ corresponds to 2eV.

In this subsection we present our calculated optical conductivities for the stoichiometric end-member LaMnO$_3$. We show that the calculated conductivities are in good agreement with experiment and that the agreement implies that LaMnO$_3$ is a Mott insulator; a more careful discussion regard to Mott insulator is given in Ref[? ].

To establish our claim we present in Fig(5) the optical conductivities for electric fields parallel to the $x - y$ plane (solid line) and perpendicular to it (dashed line) at temperatures $T = 0.16t$ (greater than $T_{oo}$), $T = 0.07t$ (below $T_{oo}$, above the magnetic ordering temperature $T_{AAF}$), and $T = 0.02t$ (roughly $0.5T_{AAF}$). The integrated optical conductivities upto

13

3eV qualitatively agree with experiments of LaMnO$_3$ [? ]. At $T = 0.16t$ we see that the conductivity has two peaks at $\omega \sim 4t$ and $8t$, and a soft gap at $\omega = 0$. If we suppress the orbital order, forcing PO/PM solution down to lower temperature, we find that the low frequency conductivity decreases [? ]. When the temperature is lowered to $T = 0.07t$ where the orbital order is well established; the peak positions remain essentially unchanged. An anisotropy produced by the orbital order appears and the gap at low frequency becomes sharper.

As the temperature is further decreased into the A-type antiferromagnetic state the peaks sharpen and the anisotropy becomes more pronounced with an increase in $\sigma_{xx}$ and a decrease in $\sigma_{zz}$ for $\omega \sim 4t$ and the converse behavior in the $\omega \sim 8t$ regime. This qualitative behavior was used by authors of Refs [? ] and [? ] to identify the lower feature as the transition to the maximal spin, orbitally disfavored final state and the higher feature as the transition to a lower spin, orbitally favored state. We make the same identification here and have adjusted the crucial parameters $U_Q$ and $U_s$ to place these peaks at the experimentally correct energies. Referring now to Fig(5)(a) we see that for these parameters the correlations are already strong enough to produce an insulating state in the absence of the long ranged order which is one characteristic of Mott insulator, although the "soft" nature of the gap places the materials close to the Mott insulator/Metal phase boundary.

### C.  Origins of Exhibited Phases

Along the temperature-descending direction, we summarize our understanding by the following statements:

(1) The staggered $Q_x$ order is a consequence of the cooperative JT effect, i.e. a combined effect from local JT interaction and lattice elastic energy.

(2) The energy difference between $(\pi, \pi, \pi)$ $Q_x$ and $(\pi, \pi, 0)$ $Q_x$ orders is very small, of the order of meV.

(3) The uniform $Q_z$ order is a consequence of the staggered $Q_x$ order, arising from the cubic term in lattice energy.

(4) The uniform $-(+)Q_z$ order reduces(enhances) the inter-layer AF coupling and decreases(increases) the Neel temperature.

To justify the first statement, we perform the calculation without cooperative Jahn-

Teller effect and obtain an orbital ordering temperature of $0.06t$ ($\sim 330$K) which is far too low compared to the observation. The cooperative Jahn-Teller coupling arising from the corner-shared octahedra facilitates the staggered $Q_x$ order. The physical picture is quite straightforward – a $Q_x$ distortion on one site induces an $-Q_x$ distortion on neighboring sites in the same $x - y$ plane.

The 2nd statement concerns the energy difference between the $(\pi, \pi, 0)$ and the $(\pi, \pi, \pi)$ $Q_x$ order. There are two possible sources. The first one is the structure in the lattice contribution. The simple form of the lattice Hamiltonian [? ] we used in our numerical calculation has the same restoring force for both distortions, but a more general form given in Eq(5) will distinguish them. Assessing this possibility requires a DFT calculation of phonon spectrum as is discussed in Ref[? ]. The second possibility is the electronic energy which we now estimate from the super-exchange (SE, essentially 2nd order perturbation) argument. The nearest neighbor ($t$) and second neighbor ($t'$) hopping processes which give rise to superexchange are illustrated in Fig(6).

In terms of the local JT splitting of $\Delta_Q$, we find that the second order superexchange calculation yields that the energy gain for both orders are $-\frac{9}{4}\frac{t^2}{\Delta_Q}$. Therefore within SE approximation, nearest neighbor hopping does not lift the degeneracy. However the second neighbor hopping does lift the degeneracy. We find that the $(\pi, \pi, 0)$ $Q_x$ state gains $-4\frac{t'^2}{\Delta_Q}$ more energy than the $(\pi, \pi, \pi)$ state. From our DFT study [? ], $t' \sim 0.035$eV and $\Delta_Q \sim$ 1.4eV, therefore the energy difference between these two orders is of the order meV which is very small compared with other energy scales in the problem. We therefore believe that the lattice effect is dominant. We model this by allowing only the $(\pi, \pi, 0)$ order in our calculation.

Within our approximation, the uniform $Q_z$ order is induced by the *local* $Q_x$ distortion via the cubic term[? ] in lattice energy, so the strength of the $Q_z$ order is proportional to $Q_x^2$. Fig(7) shows the magnitudes of the staggered $Q_x$ and uniform $Q_z$ orders at $T = 0.1t$. For these parameters we found $Q_z \sim 0.2Q_x^2$.

The 4th statement concerns the relation between the magnetic order and orbital order. In particular it is the answer to the question that in the presence of a large staggered $Q_x$ order, how a small uniform $Q_z$ order affects the magnetic order. We found that a small $+/-Q_z$ order can change the Neel temperature $T_{AAF}$ by as much as a factor of two. This effect can be qualitatively understood by comparing the effective magnetic couplings $J_i$ ($i = z$ out-
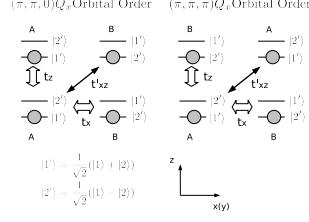
15

FIG. 6: Illustrations of superexchange processes in presence of different $(\pi, \pi, 0)$ and $(\pi, \pi, \pi)$ $Q_x$ orbital order. A and B are two sublattices occupying local orbitals $(|1\rangle + |2\rangle)/\sqrt{2}$ and $(|1\rangle - |2\rangle)/\sqrt{2}$ respectively. The hopping matrices are directional and the explicit forms are given in Ref[**?** ].
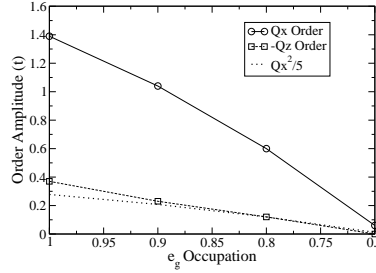


FIG. 7: The staggered $Q_x$ (solid curve) and the uniform $Q_z$ (dashed curve) orders as a function of doping at $T = 0.1t$. In the bulk, the uniform $-Q_z$ order is induced by the cubic term in lattice energy and the magnitude is proportional to $Q_x^2$. For the chosen parameters here $Q_z \sim 0.2Q_x^2$ (dotted curve).

of-plane and $x$ in-plane) for different orbital orders using super-exchange arguments. The starting point is that for each site the electron occupies the orbital $|\theta\rangle \equiv \cos\theta|1\rangle + \sin\theta|2\rangle$ $(0 < \theta < \pi)$ which is the ground state of $-(Q_z\hat{\tau}_z + Q_x\hat{\tau}_x)$. Since the strength of $Q_x$ order is at least 3 times larger than that of $Q_z$ order (see Section III G), we consider $Q_z/|Q_x|$ ranging from -0.3 to 0.3. As shown in Fig(8) in the presence of the staggered $Q_x$ order, the system is divided into two sublattices $A$ and $B$ on which the electron occupies orbital $|\theta_A\rangle$ and $|\theta_B\rangle$. Defining $\cos 2\theta = Q_z/\sqrt{Q_x^2 + Q_z^2}$, $\sin 2\theta = Q_x/\sqrt{Q_x^2 + Q_z^2}$, one finds the occupied orbitals at $A$ and $B$ are $|\theta\rangle$, $|-\theta\rangle$. Using the 2nd order perturbation, one estimates the magnetic couplings from the energy difference between FM and AF spin configurations
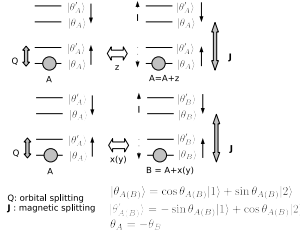
16

FIG. 8: Illustration of the $(\pi, \pi, 0)$ $Q_x$ and a uniform $Q_z$ orbital order. The local orbital states are same in $z$ direction ($|\theta_A\rangle$ or $|\theta_B\rangle$) while are alternate between $|\theta_A\rangle$ and $|\theta_B\rangle$ in the $x - y$ plane.

$(J = E_{FM} - E_{AF})$ as

$$
\begin{aligned}
J_z(\theta) &= -\frac{\cos^2 \theta \sin^2 \theta}{\Delta_{JT}} + \frac{\cos^4 \theta}{\Delta_{Hund}} + \frac{\cos^2 \theta \sin^2 \theta}{\Delta_{Hund} + \Delta_{JT}} \\
J_x(\theta) &= -\frac{3/16 + \cos^2 \theta \sin^2 \theta}{\Delta_{JT}} + \frac{\cos^2 \theta - 3\sin^2 \theta}{4\Delta_{Hund}} + \frac{3/16 + \cos^2 \theta \sin^2 \theta}{\Delta_{Hund} + \Delta_{JT}}
\end{aligned}
\tag{18}
$$

where $\Delta_{JT}$ and $\Delta_{Hund}$ are orbital and magnetic splitting respectively. From previous discussion we found $\Delta_{JT} \sim 2\mathrm{eV} \sim 4t$, $\Delta_{Hund} \sim 4\mathrm{eV} \sim 8t$. The corresponding results are given in Fig(9) where $\theta/\pi = 0.2, 0.25, 0.3$ correspond to $Q_z/|Q_x| = +0.3, 0, -0.3$ respectively. We see that for these $\theta$ values the in-plane magnetic coupling is always FM while the out-of-plane changes from FM to AF when $\theta/\pi$ varies from 0.3 to 0.2 (zero coupling at $\theta = 0.22\pi$). This SE estimate therefore implies a positive $Q_z$ order is required to produce the observed AAF order. In our DMFT calculation, we always find the AAF order at low temperature, but we indeed find the Neel temperature drastically (50%) increases when we go from small $-Q_z$ to small $+Q_z$ order. Thus the trend of variation of $T_N$ with strain is correctly captured by the superexchange calculation, but other processes also contribute the overall sign. This result indicates that the interaction is not strong enough to justify the superexchange approximation but that the superexchange results does capture one aspect of the important physics.
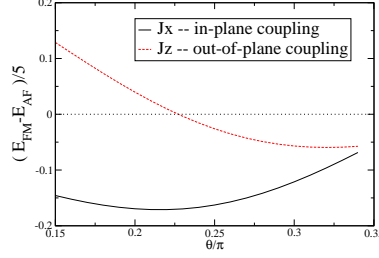
FIG. 9: (Color online) The out-of-plane ($J_z$) and in-plane ($J_x$) magnetic coupling estimated from Eqn(18) with $\Delta_{JT} = 4t$, $\Delta_{Hund} = 8t$. The negative sign favors FM coupling. $\theta = 0.25\pi$ represents the case without uniform $Q_z$ order. Positive and negative $Q_z$ orders correspond to the region $\theta < \pi/4$ and $\theta > \pi/4$ respectively.
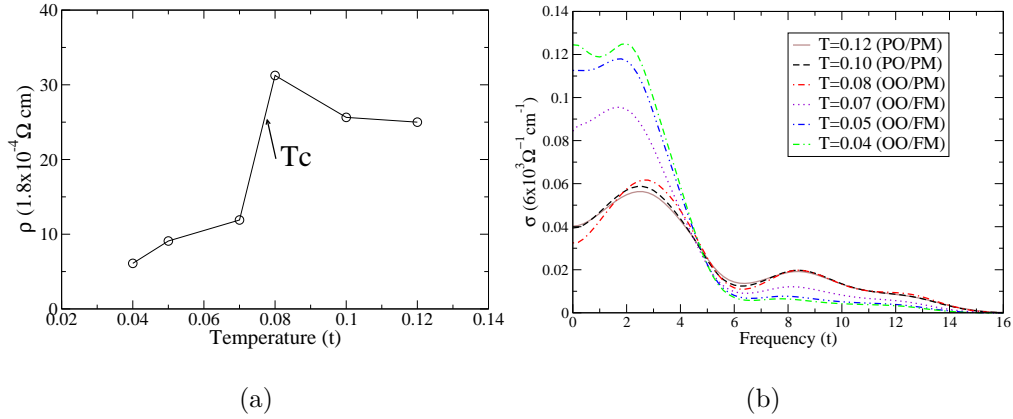


|(a)|(b)|

FIG. 10: (Color online) (a) In-plane DC resistivity $\rho_{xx}(T)$ as a function of temperature for $x = 0.3$. (b) In-plane optical conductivities for $x = 0.3$, $T = 0.12t$ to $0.04t$.

## VI. CMR REGIME AND CROSSOVER

### A. CMR Regime ($0.3 < x < 0.5$)

We choose $x = 0.3$ ($N = 0.7$) as being representative of the CMR region. For this doping, the system goes from PO/PM to PO/FM around $275K$. The transition is accompanied by an insulator/metal transition which is shown in Fig(1) of Chapter 1 in Ref[? ]. At this transition the $d\rho/dT$ changes sign. Fig(10)(a) shows the calculated $\rho(T)$. We indeed find a M/I transition across the Curie transition. This M/I transition is also reflected in the optical conductivities shown in Fig(10)(b). Our calculations qualitatively agree with the experimental data of $La_{0.7}Ca_{0.3}MnO_3$. To be more quantitative, Table I compares the kinetic energy defined as $K = (\frac{\hbar a}{e^2})\frac{2}{\pi} \int_0^{2.7eV} \sigma(\omega)d\omega$ obtained from both experiments [? ] and our

theoretical calculation. The reasonable agreement suggests that our model well captures the main physics (right degree of freedom and reasonable effective interactions) below 2.7eV. However there are several differences between calculation and data. First the experimental values are systematically larger. Two reasons are that the experiments inevitably involve transition from lower oxygen bands to Fermi level which is not included in our model and our calculation yields orbital order at low T which does not occur in the actual material. In addition our calculation overestimates the density of states around zero frequency at high temperature PM phase. In terms of DC resistivity, it means the high-T PM phase is not insulating enough. We shall discuss the possible physics accounting for this inconsistency later.

| | Expt (Ref[?]) | Calculation |
|---|---|---|
| FM | 0.22 | 0.152 ($T = 0.04t$) |
| PM | 0.1 | 0.076 ($T = 0.1t$) |

Table I: Kinetic energy in the unit of eV obtained from both experiments and our calculation, using $t = 0.5$eV.

One issue from earlier calculations is that the $T_c$ for pure DE model is roughly 3 times higher than the observed one[?]. The Curie temperature $T_c$ with $J_{AF} = 0$ obtained here (roughly $0.08t$) is $\sim 40\%$ lower than that of [?]. Introducing G-type AF coupling $J_{AF}(\sim 0.01t$ from our fit) further reduces $T_c$ to $0.075t \sim 412K$, not too far from the experimental value $\sim 275K$. We expect that a large fraction of the remaining difference arises from spatial and thermal fluctuation effects not captured by our mean field theory.

**B.  The Crossover Regime** ($0.1 < x < 0.3$)

In this doping range, when the temperature is lowered, the system goes from PO/PM to OO/PM, then to OO/FM phase and we take $x = 0.2$ ($N = 0.8$) as a representative doping. In this region, both cooperative JT and DE mechanisms are important. These two mechanisms are competing and not compatible in the following sense – the cooperative JT tends to break the in-plane symmetry which facilitates the staggered $Q_x$ order and localizes electrons, while the DE wants the system to be uniform and delocalizes electrons. This competition is shown in Fig(11)(a) where the magnitude of the staggered $Q_x$ order is plotted. We find that when lowering the temperature, the magnitude of $Q_x$ order increases above

19

the Curie temperature, and then quickly saturate below $T_c$. If we force the PM solution at low temperature, then the staggered $Q_x$ order keeps on increasing as T is decreased. This is consistent with the pair distribution function (PDF) measurements [**?** ] which show below the Curie temperature at $x = 0.25$, the peak associated with JT distortion decreases when lowering the temperature. Fig(11)(b) shows the resistivity as a function of temperature. We see that the system is an insulator at high temperature and a downturn in $\rho(T)$ happens at the Curie temperature, below which DE effects gradually takes over and the system is metallic. Finally we point out that around $x = 0.3$, $T_{oo}$ and $T_c$ happen around the same temperature (around $0.1t$ in Fig(4)). We do not resolve the behavior around this point carefully
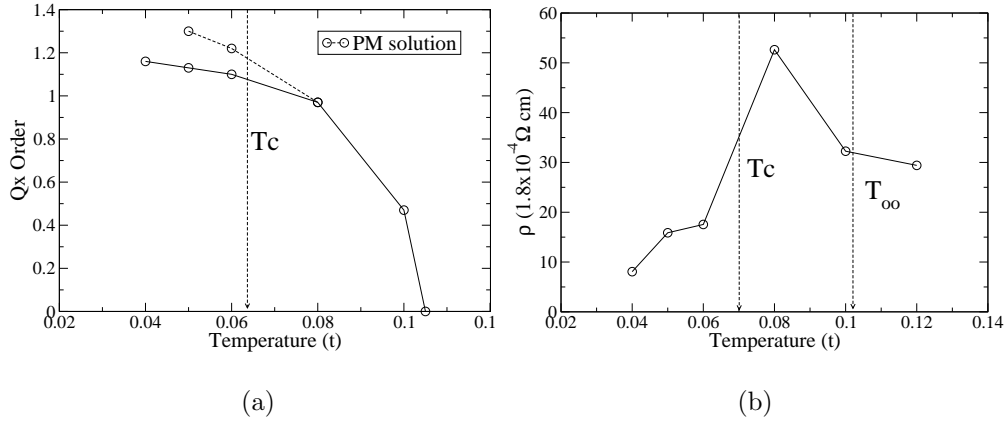


(a)                                         (b)

FIG. 11: (a) The amplitude of staggered $Q_x$ order as a function of temperature. The dashed curve are calculated at paramagnetic phase. (b) Resistivity for $x = 0.2$ ($N = 0.8$) as a function of temperature. The vertical dashed lines indicate the transition temperatures.

## VII.   DISCUSSION

### A.   Summary

With a fixed set of parameters, our calculations semiquantitatively produce the observed phase diagram – the relative positions of magnetic and orbital orders in the doping-temperature plane are consistent with experiments. In particular the magnetic transition temperatures (both Neel and Curie temperatures) are in reasonable agreement with data with calculated values being about 1.5 times higher than the measured values. Some part

of the difference arises from the fluctuation corrections to the mean field theory, which are typically of the order of 30% in three dimension. As for the excitation spectra, our results are consistent with observed optical conductivity. In particular we reproduce the peak positions (this is how we fit some of the parameters) and the corresponding amplitudes for a wide range of doping and temperature. We believe these agreements to experiments indicate that our model and fittings capture the essential physics of the manganite problem. In this section we give a more detailed discussion on several issues and on inconsistencies to data regarding to our results.

## B.   Role and Effect of GdFeO$_3$ Rotation

Our results indicate the local interaction strength is only slightly stronger than the critical value of Mott transition [? ]  implying the system is very sensitive the hopping $t$. As discussed in Ref[? ? ], the hopping is very sensitive to the structure. In particular the manganites form in a distorted version of the ideal perovskite structure. The most important important distortion appears to be a GdFeO$_3$-type rotation which buckles the Mn-O-Mn bond. Table II summarizes the relation between the bond angle, the cation composition, and the hopping. For a perovskite material AMnO$_3$, the Mn-O-Mn bond-angle as a function of A-site composition is taken from Ref[? ] and the corresponding hoppings are calculated in Ref[? ]. From this table we infer that using the same hopping $t = 0.5$eV for LaMnO$_3$ and Ca doped manganite is reasonable, but is not for Sr-doped.

| A-site | bond-angle | hopping (ratio) |
|---|---|---|
| La$_1$ Ideal | 180 | 0.65eV (1) |
| La$_{0.7}$Sr$_{0.3}$ | 166 | 0.58eV (0.9) |
| La$_{0.7}$Ca$_{0.3}$ | 160 | 0.53eV (0.81) |
| La$_1$ Real | 155 | 0.5eV (0.78) |

Table II: The composition of A-site elements, its corresponding Mn-0-Mn angle and effective hopping $t$.

In Ref[? ], we show that for $t = 0.65$eV LaMnO$_3$ is not a Mott insulator. When using $t = 0.6$eV to simulate La$_{0.7}$Sr$_{0.3}$MnO$_3$, we find that (1) the Curie temperature increases from $\sim 420$K ($t = 0.5$eV) to $\sim 530$K (shown in the dashed curve in Fig(4)) and (2) the high temperature PO/PM phase becomes almost metallic ($d\rho/dT$ is very flat, and the minimum
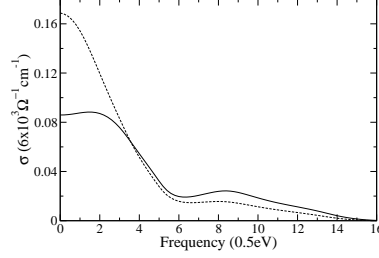
FIG. 12: The optical conductivities calculated for parameters which simulate $La_{0.7}Sr_{0.3}MnO_3$. Solid and dashed curves are computed above and below the Curie temperature. To convert the frequency into physics units [eV], divide the x-axis by two.

around $\sigma(\omega = 0)$ almost vanishes). The optical conductivities for $t = 0.6$eV for two temperatures, just above and below $T_c$, are shown in Fig(12). Both of our findings ($T_c$ and $\sigma(\omega)$) are consistent with the difference between $La_{0.7}Sr_{0.3}MnO_3$ and $La_{0.7}Ca_{0.3}MnO_3$ reported in Ref[**?** ]. We emphasize, however, that the main message here is that for the given local interaction strength, the system is very sensitive to the bandwidth and any uncertainty in estimating parameters could easily drive the system to either Mott insulating or metallic phases.

## C.   Orbital Ordering

We found that with our standard parameters, the calculated $T_{oo}$ decreases too slowly as a function of doping $x$ (see Fig(4)). Fine tuning parameters (e.g. varying $\epsilon$ and $U_Q$) can correct this problem but this degree of data fitting is somewhat arbitrary so we do not persue it here.

However, we point out that using our standard parameters, the orbitally disordered and orbital ordered phases behave very similarly as far as the excitation is concerned. To demonstrate this we show in Fig(13) the optical conductivities for $x = 0.3$, $T = 0.08t$ at both OO and PO phases. One sees that the difference is very limited. Furthermore we found the Curie temperature obtained from these two phases are very close (difference $< 5\%$). These results suggest that the crucial electronic physics is controlled by local distortions which (because the correlations are strong) are well formed. The important effect caused by the orbital order is actually the uniform $Q_z$ order which introduces an isotropy to the system
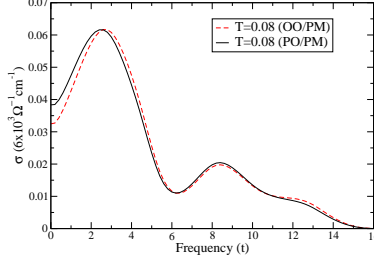
FIG. 13: (Color online) The optical conductivities calculated at $x = 0.3$, $T = 0.08t$ for PO (solid) and OO (dashed) phases.

and whose sign substantially affects the Neel temperature for the undoped case.

We also mention here that the effective Mn-Mn hopping being through oxygen $p$ orbitals also introduces an intersite orbital coupling [? ] which is very similar to the cooperative JT effect and is referred to as the "charge-transfer" mechanism. This can be understood from the super-exchange argument where we consider a simple Mn-O-Mn system and compare energies of different orbital configurations by the perturbation expansion of the Mn-O hopping $t_{pd}$ [? ]. In the model where the oxygen orbitals are not included, those "virtual processes" lead to an spin-independent orbital-exchange interaction [? ] as

$$H_{o-ex} = A \sum_{i,\alpha=x,y,z} I_i^\alpha I_{i+\alpha}^\alpha \qquad (19)$$

with $I^z = \tau_z$, $I^x = -\frac{1}{2}\tau_z - \frac{\sqrt{3}}{2}\tau_x$, $I^y = -\frac{1}{2}\tau_z + \frac{\sqrt{3}}{2}\tau_x$, and $A$ a *positive* coefficient. The simple mean field approximation to the term produces an external field on site o as

$$
\begin{aligned}
H_{o-ex} &= A \sum_{\alpha=x,y,z} I_o^\alpha (\langle I^\alpha \rangle_{+\alpha} + \langle I^\alpha \rangle_{-\alpha}) \\
&= A \left[ \tau_z \frac{1}{\sqrt{6}} (2E_z - E_x - E_y) + \tau_x \frac{1}{\sqrt{2}} (-E_x + E_y) \right]
\end{aligned}
\qquad (20)
$$

with $E_z = \frac{2}{\sqrt{6}} \sum_{\alpha=\pm z} \langle \tau_z \rangle_\alpha$ and $E_{x(y)} = \frac{-1}{\sqrt{6}} \sum_{\alpha=\pm x(\pm y)} [\langle \tau_z \rangle_\alpha + (-)\sqrt{3}\langle \tau_x \rangle_\alpha]$. which is of the same form of the cooperative JT effect derived in the appendix. Therefore in our approximation where the orbital order and structural JT distortions are equivalent, including the charge-transfer mechanism amounts to a reinterpretation of our cooperative JT parameter $\epsilon = 2A$ and does not change any results.

23

### D. High-T Insulating Phase

Using the standard parameters, our calculation obtains an insulating behavior at high T PO/PM phase for doping ranging from $x = 0$ to $x \sim 0.4$. With the semiclassical approximation, the electron-electron interaction is replaced by some classical fields and the impurity problem becomes polaron-like [? ? ]. The high T insulating phase away from zero doping should be therefore interpreted as a phase separation between $N = 1$ orbitally fully-polarized state and $N = 0$ state. Since our estimate indicates [? ] the on-site Coulomb interaction is roughly three times stronger than the electron-lattice, the semiclassical method may overestimate the insulating behavior under single-site DMFT approximation.

The other issue is that compared to the experiments, our calculations overestimate the optical conductivity around zero frequency at high temperature PO/PM phase. This might be due to short-ranged correlations not included in the single site DMFT approximation. According to recent cluster DMFT studies of the 1-band Hubbard model [? ? ], including the short-range correlation significantly reduces the low energy density of states. We also observe that in doped CMR systems there is a strong empirical association between insulating behavior ($d\rho/dT < 0$ with $\rho$ DC resistivity and $T$ temperature) and strong short-ranged Jahn-Teller (polaron glass) order [? ? ? ]. Including spatial correlations beyond the single site approximation is an important topic for future regard.

### E. Missing Phases

Our calculation misses two phases. First around $x = 0.5$, a charge ordered (CO) phase occurs, accompanied by one particular orbital and magnetic order called CE phase [? ] which requires a very large unit cell ($4 \times 4$) in the $x - y$ plane. Our in-plane unit cell is not large enough to include this phase. However at $x = 0.5$ we do find that the convergence becomes more and more difficult when lowering the temperature (below $T = 0.04t$) which may be an indication of CE phase. Second, around $x = 0.1 - 0.2$ we do not get the FM insulating phase at low temperature.

## F.  Limits of Approximation

Now we discuss the limits of our approximation. First we discuss the breathing mode polaron effect. In the current approximation the breathing mode coupling is treated in simple mean field and therefore has no effect in the charge-uniform phase. To include the breathing mode polaron, one has to consider the fluctuation of the breathing-mode distortion by integrating over $Q_0$ field when computing the impurity model [**?** ]. Since the real time-consuming computation involved in our approach is doing multi-dimensional integral (see Section III.F), performing an additional integral is now beyond our computational power. It is possible that the breathing mode polaron is also crucial for the charge order at $x = 0.5$. Since with breathing mode polarons electrons are already localized but just randomly distributed at high temperature (therefore the system is not charge-uniform, but can be treated within single-site DMFT [**?** ]), the CO is then formed at low temperature to gain more energy from the gap. Without the polaron to localize electrons, it is very hard to get CO (usually it requires some nesting in the band structure which is not the case here).
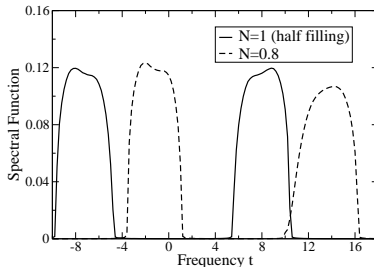


FIG. 14:  Spectral function calculated for one-band Hubbard model for bandwidth $6t$, on-site $U = 16t$ at $T = 0.1t$. For both half filling (solid) and $N = 0.8$ (dashed), the lower and upper bands have the equal weights.

Finally we point out that the SCA does not treat the quantum physics of the Mott insulator faithfully. To be specific, we take 1-band Hubbard model with strong coupling as an example. With the SCA the metal/insulator transition occurs at $U \sim U_{c1}$ so the effect pf the Kondo peak is absent. Further, independent of doping $x$, the upper and lower Hubbard bands have the same weight with SCA while in the reality, the upper Hubbard band represents adding one electron to the *occupied* site the whose weight is ought to be 1-$x$. This consideration implies the SCA works well at half filling and becomes less reliable away from it. This is illustrated in Fig(14) which show the spectral functions for $N = 1$

(half-filling) and $N = 0.8$. We see that in both cases the upper and lower bands have the same weight. For our 2-band manganite model in the strong coupling limit, the SCA solution for PO/PM phase results in 4 bands with weights 1-$x$, 1+$x$, 1+$x$, 1-$x$ (from low energy to high) respectively. However the 3rd peak corresponds to adding one electron to the state with same orbital but opposite spin whose weight should be 1-$x$. Based on the same argument we conclude that the SCA for 2-band model is more reliable without doping than with doping. A more accurate treatment of the doped phase requires an improved, fully quantum impurity solver.

## VIII.   CONCLUSION

A general model for bulk manganite, including electron-electron, electron-phonon, and phonon-phonon interactions is formulated and solved by semiclassical approximation. Our calculation is qualitatively good in the sense that it yields the right distribution of phases in the $(x, T)$ plane and produces the correct low energy excitations as described in section 2.5.2. The physical origin of each exhibited phase is identified within our model. For the LaMnO$_3$ below $T_{oo}$, the exhibited in-plane staggered $Q_x$ order is mostly driven by the cooperative Jahn-Teller (lattice effect) rather than the pure electronic effect while the uniform $-Q_z$ order is a consequence of the anharmonic term in lattice energy. Our results indicate that the local interaction strength is only slightly stronger than the critical value for Mott transition and the system is consequently very sensitive to mechanisms controlling the effective bandwidth. With this local interaction strength, the orbitally ordered and orbitally disordered phases behave very similarly. As the doping increases, the electrons start to delocalize and after $x > 0.3$, the double-exchange mechanism dominates so orbital order vanishes and the system has the FM/Metallic ground state.

Discrepancies between our calculation and the observations are also carefully discussed. In particular our calculations overestimate the optical conductivity around zero frequency at high-temperature insulating phase. This inconsistency leads us to conclude that the key physics we are missing in the calculation is the short-ranged correlation. In the future we will include the short-ranged correlation and also adopt a better impurity solver for this problem.

## IX.  ACKNOWLEDGMENT

## APPENDIX A: THE VALIDITY OF SEMICLASSICAL APPROXIMATION

In this appendix we examine the validity of the semiclassical approximation by comparing the excitation spectrum computed using the SCA results to the exact eigenstates of the local Hamiltonian. As discussed in Section II, we assume that the crystal field (ligand field) is large enough that the $t_{2g}$ levels are in their maximum spin state and that the pair hopping between $t_{2g}$ and $e_g$ orbitals is quenched. In this case the on-site Hamiltonian in the $e_g$ manifold is

$$H_{loc} = \sum_{\sigma,\sigma'}(U - J)n_{1,\sigma}n_{2,\sigma'} + U\sum_{i=1,2}n_{i,\uparrow}n_{i,\downarrow} + J(c^{\dagger}_{1,\uparrow}c^{\dagger}_{1,\downarrow}c_{2,\downarrow}c_{2,\uparrow} + h.c.)$$
$$- 2J\vec{s}_1 \cdot \vec{s}_2 - 2J_H\vec{S}_c \cdot (\vec{s}_1 + \vec{s}_2) + \Delta(n_1 - n_2) \tag{A1}$$

Here $\vec{s}_i = \sum_{\alpha\beta}c^{\dagger}_{i\alpha}\vec{\sigma}_{\alpha\beta}c_{i\beta}$, $\vec{S}_c$ has magnitude 3/2 and $\Delta$ is the crystal field splitting arising from the long-range Jahn-Teller order. In spherical symmetry $J_H = J$; we assume this henceforth. The eigenstates are characterized by the particle number, total spin and total $e_g$ spin, and the orbital configuration. There are 16 1-electron and 24 2-electron eigenstates, taking the configurations of the core spin into account.

To compare the exact solution of the local Hamiltonian to experiment and the semiclassical calculation, we need the quantity $\Delta E(S) = E(n = 2, S) + E(n = 0, S = 3/2) - 2E(n = 1, S = 2)$ which gives the locations of peaks in the optical conductivity in the atomic limit. The following table lists the eigenstates and the corresponding transition energies.

| States | $\Delta E$ | Semiclassical |
|---|---|---|
| $^3A_2(5/2)$ (6) | $U - 3J/2 + 2\Delta$ | $2U_Q$ |
| $^3A_2(3/2)$ (4) | $U + 7J/2 + 2\Delta$ | $2(U_s + J_H) + 2U_Q$ |
| $^3A_2(1/2)$ (2) | $U + 13J/2 + 2\Delta$ | not accessible |
| $^1E^-(3/2)$ (4) | $U + 9J/2 + 2\Delta - \sqrt{4\Delta^2 + J^2}$ | $2(U_s + J_H)$ |
| $^1A(3/2)$ (4) | $U + 9J/2 + 2\Delta + \sqrt{4\Delta^2 + J^2}$ | not accessible |
| $^1E^+(3/2)$ (4) | $U + 7J/2 + 2\Delta$ | $2(U_s + J_H) + 2U_Q$ |

Table III: The 2-electron eigenstates and

the corresponding transition energies

Determining the coupling strength in Eq(A1) by fitting the optical data [? ] is described in detail in Ref[? ]. Here we simply quote the results, $U = 2.3 \pm 0.3$eV, $2\Delta \sim J \sim 0.5$eV. Following the analysis and notations in Ref[? ], there are three optical peaks located at

$$
\begin{aligned}
\Delta E_{HS} &= U - 3J/2 + 2\Delta \\
\Delta E_{LS}^- &= U + 9J/2 + 2\Delta - \sqrt{4\Delta^2 + J^2} \\
\Delta E_{LS}^+ &= U + 7J/2 + 2\Delta
\end{aligned}
\tag{A2}
$$

We now compare this result to the semiclassical calculation. From Fig(5) we observe three peaks in the optical conductivity: a low-lying peak at energy $2U_Q$ which we identify with $\Delta E_{HS}$, an intermediate peak at energy $U_s + J_H$ which we identify with $\Delta E_{LS}^{\bar{J}T}$, and a higher peak at the sum of these energies. This highest peak represents physically the states $^1E^+(3/2)$ and $^3A_2(3/2)$ where both orbitals are occupied while the total spin (including the core spin) is $3/2$. The $^3A(3/2)$ state in large $\Delta$ limit represents a state where both electrons occupy energy-disfavored orbital which cannot be reached by a single hopping and has no correspondence in the SCA. It is the defect of the semiclassical approximation that the highest peak is too high in energy. However this defect is not serious because the high-lying states are not important for our analysis.

**APPENDIX B: EFFECTIVE POTENTIAL**

In this appendix, we describe in detail how we encode the inter-site lattice coupling into the single-site impurity problem. The basic logic is the following. First we write down the energy functional for the *lattice* problem in terms of fields labeled by site index $\phi_i$ which couples to some local quantity $\rho_i$, then the *local* partition function is obtained by integrating out all fields except the field at origin site $\phi_0$. The long-range order corresponds to some spatial pattern of $\rho_i$ which generates an extra coupling to local field $\phi_0$. This extra coupling depends on the long-range order containing information from **other** sites $\rho_i$ $i \neq o$. We first give a general functional for lattice elastic energy then work out 1-dimensional case explicitly with a specific lattice model. Finally we derive the formalism used in our calculation.

### 1. General Functional of Elastic Energy

The goal here is to derive the elastic energy in terms of three even-parity $MnO_6$ distortion modes. As mentioned in the text, the lattice degree of freedom includes oxygen motion along Mn-O bond $u_i$ and manganese general displacement $\vec{\delta_i}$. Assuming the spring constant between adjacent Mn-O is $1/K_1$, a general elastic energy is

$$
\begin{aligned}
E_{lat} = {} & \frac{1}{2K_1} \sum_{i,a} [(\delta_i^a - u_i^a)^2 + (\delta_i^a - u_{i-1}^a)^2] \\
& + \frac{1}{2} \sum_{\vec{k},ab} E^{ab}(\vec{k}) \delta_{\vec{k}}^a \delta_{-\vec{k}}^b + \frac{1}{2} \sum_{\vec{k},ab} D^{ab}(\vec{k}) u_{\vec{k}}^a u_{-\vec{k}}^b \\
= {} & \frac{1}{K_1} \sum_{\vec{k},a} [\delta_{\vec{k}}^a \delta_{-\vec{k}}^a + u_{\vec{k}}^a u_{-\vec{k}}^a - (1 + e^{+ik_a}) u_{\vec{k}}^a \delta_{-\vec{k}}^a] \\
& + \frac{1}{2} \sum_{\vec{k},ab} E^{ab}(\vec{k}) \delta_{\vec{k}}^a \delta_{-\vec{k}}^b + \frac{1}{2} \sum_{\vec{k},ab} D^{ab}(\vec{k}) u_{\vec{k}}^a u_{-\vec{k}}^b
\end{aligned}
\tag{B1}
$$

where $E^{ab}(\vec{k})$, $D^{ab}(\vec{k})$ represent general harmonic coupling Mn-Mn, O-O displacements, and $a,b$ sums over $x,y,z$. To get rid of the Mn motions, we use the saddle point approximation $\frac{\partial E_{lat}}{\partial (\delta_{-\vec{k}}^a)} = 0$ which leads to

$$
\delta_{\vec{k}}^a = \frac{1}{2K_1} \sum_b [\underline{I} + \underline{E}(\vec{k})/2]_{ab}^{-1} (1 + e^{ik_b}) u_{\vec{k}}^b
\tag{B2}
$$

and the lattice energy in this approximation is $E_{lat} = \sum_{\vec{k},ab} u_{\vec{k}}^a \tilde{m}^{ab}(\vec{k}) u_{-\vec{k}}^b$ with

$$
\tilde{m}^{ab}(\vec{k}) = \frac{\delta^{ab}}{K_1} - \frac{1}{4K_1^2}(1 + e^{-ik_a})[\underline{I} + \underline{E}(\vec{k})/2]_{ab}^{-1}(1 + e^{ik_b}) + \frac{1}{2} D^{ab}(\vec{k})
\tag{B3}
$$

Defining strain variables $v_i^a = u_i^a - u_{i-a}^a$, $v_{\vec{k}}^a = u_{\vec{k}}^a(1 - e^{-ik_a})$, we express $E_{lat}$ in terms of $v_{\vec{k}}^a$ which is

$$
E_{lat} = \sum_{\vec{k},ab} v_{\vec{k}}^a m^{ab}(\vec{k}) v_{-\vec{k}}^b
\tag{B4}
$$

where $m^{ab}(\vec{k}) = \frac{1}{1-e^{-ik_a}} \tilde{m}^{ab}(\vec{k}) \frac{1}{1-e^{ik_b}}$. The advantage of expressing $E_{lat}$ in strain variables is that they are closer to the even-parity distortion modes defined in Eqn(6). $m^{ab}(\vec{k})$ allows us to estimate the proximity effect for structural order. In particular if we are interested in how $(\pi, \pi, 0)$ $Q_x$ order propagates along $z$ direction, then the quantity to study is $m^{ab}(\pi, \pi, k_z)$. The explicit form of $m^{ab}(\vec{k})$ is model-dependent and here we only consider spring constants between adjacent Mn-O $(1/K_1)$ and Mn-Mn $(1/K_2)$ which are of most importance.

## 2. 1 Dimensional Mn-O Chain

Now we explicitly work out the local effective potential in the 1-dimensional case. The procedure is outlined here. We first adopt the procedure described in the previous subsection to express (with saddle point approximation) the elastic energy in terms of strain variables in real space $v_i$. Then the effective potential is obtained by integrating out all $v_i$ except the one at origin $v_0$. For 1D Mn-O chain, we drop the index $a, b$ since there is only one direction and the elastic lattice energy is

$$
\begin{aligned}
E_{lat} &= \frac{1}{2K_1} \sum_i [(\delta_i - u_i)^2 + (\delta_i - u_{i-1})^2] + \frac{1}{2K_2} \sum_i (\delta_{i+1} - \delta_i)^2 \\
&= \frac{1}{K_1} \sum_k [u_k u_{-k} + \delta_k \delta_{-k} - u_k \delta_{-k}(1 + e^{ik})] + \frac{2}{K_2} \sum_k \sin^2(k/2) \delta_k \delta_{-k}
\end{aligned}
\tag{B5}
$$

For this case, $\frac{E(k)}{2} = \frac{2}{K_2} \sin^2(k/2)$ and $D(\vec{k}) = 0$. The saddle point approximation $\frac{\partial E_{lat}}{\partial \delta_{-k}} = 0$ implies

$$
\delta_k = \frac{u_k(1 + e^{ik})}{2 + 4\bar{K} \sin^2(k/2)}
\tag{B6}
$$

where $\bar{K} = K_1/K_2$. The effective energy functional $E_{lat}$ (as a function of $u_k$ only) is therefore

$$
\begin{aligned}
E_{lat} &= \frac{2\bar{K}+1}{K_1} \sum_k \frac{\sin^2(k/2)}{1 + 2\bar{K} \sin^2(k/2)} u_k u_{-k} \\
&= \frac{2\bar{K}+1}{4K_1} \sum_k \frac{1}{1 + 2\bar{K} \sin^2(k/2)} v_k v_{-k}
\end{aligned}
\tag{B7}
$$

To see how local strains at different sites couple to one another, we express $E_{lat}$ in the real space $v_i$.

$$
\begin{aligned}
E_{lat} &= \frac{2\bar{K}+1}{4K_1} \sum_k \frac{1}{1 + 2\bar{K} \sin^2(k/2)} v_k v_{-k} \\
&= \frac{1}{N} \frac{2\bar{K}+1}{4K_1} \sum_{i,j} \sum_k \frac{e^{ik(r_i - r_j)}}{1 + 2\bar{K} \sin^2(k/2)} v_i v_j \\
&= \frac{2\bar{K}+1}{4K_1} \sum_{i,j} f(i - j) v_i v_j
\end{aligned}
\tag{B8}
$$

where $f(i - j) = \frac{1}{N} \sum_k \frac{e^{ik(i-j)}}{1 + 2\bar{K} \sin^2(k/2)} = \frac{1}{2\pi} \int_{-\pi}^{\pi} dk \frac{\cos(kn)}{1 + 2\bar{K} \sin^2(k/2)}$ ($\sum_k \to \frac{N}{2\pi} \int_{-\pi}^{\pi} dk$ for lattice constant $a = 1$). For this simple model, the integral can be done analytically (the most straightforward way may be changing variable $z = e^{ik}$ and then using the residue theorem!).

By defining $\alpha = 1 + K_2/K_1$, $E_{lat}$ becomes

$$E_{lat} = \frac{2\bar{K}+1}{4K_1}\sqrt{\frac{\alpha-1}{\alpha+1}}\sum_{i,j}(\alpha-\sqrt{\alpha^2-1})^{|i-j|}v_iv_j$$

$$= \frac{1}{2K}\sum_{i,j}\epsilon^{|i-j|}v_iv_j \qquad (B9)$$

where $K = 2K_1/\sqrt{2\bar{K}+1}$, and $\epsilon = \alpha - \sqrt{\alpha^2-1} < 1$. Note that the coupling between local strains is exponentially decay since $\epsilon^n = e^{-a|n|}$ with $a = -\ln\epsilon$.

Including the the electron-lattice coupling $\sum_i h_iv_i$, the total energy is

$$E = E_{lat} + E_{e-l} = \sum_{ij}A_{ij}v_iv_j + \sum_i h_iv_i \qquad (B10)$$

where $h_i$ in this case is the charge density at site $i$. The effective potential at site 0 is given by integrating out the degrees of freedom of all other sites $v_1, v_2, ..., v_N$, i.e.

$$\int dv_0 e^{-V_{eff}(v_0)} = \int dv_0 e^{-A_{00}v_0^2}\int dv_1..dv_N \exp[-\sideset{}{'}\sum A_{0i}v_0v_i - \sideset{}{'}\sum A_{ij}v_iv_j - \sideset{}{'}\sum h_iv_i]$$

$$= \int dv_0 \exp[-(A_{00}-\frac{1}{4}\sideset{}{'}\sum A_{0i}A_{ij}^{-1}A_{0j})v_0^2 + \frac{1}{2}\sideset{}{'}\sum h_jA_{ij}^{-1}A_{0i}v_0 + \frac{1}{4}\sideset{}{'}\sum h_iA_{ij}^{-1}h_j]$$

where $\sum'$ means site 0 is excluded in the summation.

The effective potential is

$$V_{eff}(v_0) = Dv_0^2 - \frac{1}{2}\sideset{}{'}\sum h_jA_{ij}^{-1}A_{0i}v_0 + \text{const} \qquad (B11)$$

where $D = A_{00} - \frac{1}{4}\sum' A_{0i}A_{ij}^{-1}A_{0j}$. We see that the charge density at site $h_i(i \neq 0)$ also contribute to the "external" field coupling to $v_0$.

### 3.  3 Dimensional Case

The 1D result can be easily generalized to the 3D case. For the model we considered, the lattice energy in $k$ space is

$$E_{lat} = \frac{2\bar{K}+1}{4K_1}\sum_{a=x,y,z}\sum_{k_a}\frac{1}{1+2\bar{K}\sin^2(k_a/2)}v_{k_a}v_{-k_a} \qquad (B12)$$

From this expression, we find that in our simple model there is no proximity effect for $(\pi,\pi,0)$ order of any kind since there is no coupling between different components of $\vec{k}$. We also

notice that the energy cost is at its minimum when $k_a = \pi$ (staggered order of any kind), therefore at integer occupancy the system prefer some staggered long-range order since the staggered order lowers electronic energy.

Assuming $\epsilon$ is small thus only including the nearest neighbor coupling, the lattice energy in real space is

$$E_{lat} = \frac{1}{2K} \sum_{i,a=x,y,z} [(v_i^a)^2 + 2\epsilon v_i^a v_{i+a}^a] \tag{B13}$$

One can also express $E_{lat}$ in three $MnO_6$ even parity modes $Q$ by the following transformation

$$\begin{pmatrix} Q_{i,0} \\ Q_{i,x} \\ Q_{i,z} \end{pmatrix} = \begin{pmatrix} \frac{1}{\sqrt{3}} & \frac{1}{\sqrt{3}} & \frac{1}{\sqrt{3}} \\ \frac{1}{\sqrt{2}} & -\frac{1}{\sqrt{2}} & 0 \\ -\frac{1}{\sqrt{6}} & -\frac{1}{\sqrt{6}} & \frac{2}{\sqrt{6}} \end{pmatrix} \begin{pmatrix} v_{i,x} \\ v_{i,y} \\ v_{i,z} \end{pmatrix} \equiv U \begin{pmatrix} v_{i,x} \\ v_{i,y} \\ v_{i,z} \end{pmatrix}$$

However it is more convenient to work in stain field $v$ until we obtain the local effective potential which will be expressed in $Q$.

The electronic source fields $h_i$ are defined as

$$\begin{aligned} h_{i,0} &= \langle e_{ab} c_{i,a}^\dagger c_{i,b} \rangle \\ h_{i,x} &= \langle \tau_{ab}^x c_{i,a}^\dagger c_{i,b} \rangle \\ h_{i,z} &= \langle \tau_{ab}^z c_{i,a}^\dagger c_{i,b} \rangle \end{aligned}$$

and the local electron-lattice coupling is

$$E_{JT} = -h_0 Q_0 - (h_x Q_x + h_z Q_z) = -(v_x H_x + v_y H_y + v_z H_z) \tag{B14}$$

with

$$\begin{aligned} H_x &= \frac{1}{\sqrt{3}} h_0 + \frac{1}{\sqrt{2}} h_x - \frac{1}{\sqrt{6}} h_z \\ H_y &= \frac{1}{\sqrt{3}} h_0 - \frac{1}{\sqrt{2}} h_x - \frac{1}{\sqrt{6}} h_z \\ H_z &= \frac{1}{\sqrt{3}} h_0 + \frac{2}{\sqrt{6}} h_z \end{aligned} \tag{B15}$$

Following the procedure for 1-dimensional case, the effective potential at the origin site is therefore

$$\begin{aligned} V_{eff} &= D(v_x^2 + v_y^2 + v_z^2) + \frac{1}{2} \vec{E} \cdot \vec{v} \tag{B16} \\ &= D(Q_0^2 + Q_x^2 + Q_z^2) + \frac{\epsilon}{2} \vec{F} \cdot \vec{Q} \tag{B17} \end{aligned}$$

with $E_{x(y,z)} = \sum' H_{j_{x(y,z)},x(y,z)} A^{-1}_{i_{x(y,z)},j_{x(y,z)}} A_{0,i_{x(y,z)}}$ and $\vec{F} = U\vec{E}$. $i_{x(y,z)}$ labels the sites along $x(y,z)$ axis. We call $\vec{F}$ effective external field. Keeping only the linear term in $\epsilon$, we have

$$D = \frac{1}{2K}(1 - \epsilon^2/4) \sim \frac{1}{2K} \tag{B18}$$

$$E_x = H_{+\hat{x},x} + H_{-\hat{x},x}$$

$$E_y = H_{+\hat{y},y} + H_{-\hat{y},y}$$

$$E_z = H_{+\hat{z},z} + H_{-\hat{z},z} \tag{B19}$$

$$\tag{B20}$$

and $\vec{F} = \left( \frac{1}{\sqrt{3}}(E_x + E_y + E_z), \frac{1}{\sqrt{2}}(E_x - E_y), \frac{1}{\sqrt{6}}(-E_x - E_y + 2E_z) \right)$.